

AVION: Aerial Vision–Language Instruction from Offline Teacher to Prompt-Tuned Network

Yu Hu^{1*} Jianyang Gu^{2*} Hao Liu¹ Yue Cao¹ Jozsef Hamari³ Zheng Liu^{1†} Mohsen Zardadi^{3†}

¹The University of British Columbia, Okanagan, Kelowna, BC, Canada

²The Ohio State University, Columbus, OH, USA

³TerraSense Analytics, Kelowna, BC, Canada

yu.hu@ubc.ca, gu.1220@osu.edu, hao.liu@ubc.ca, yue.cao@ubc.ca

{jozsef.hamari, mohsen.zardadi}@terrasense.ca, zheng.liu@ubc.ca

Abstract

Adapting vision-language models to remote sensing imagery remains challenging due to two key factors: limited semantic coverage in textual representations and insufficient adaptability of visual features. These issues are particularly significant in aerial scenes, which involve various visual appearances and fine-grained object distinctions. We propose AVION, a knowledge distillation framework tailored for remote sensing adaptation of vision-language models. The teacher module constructs semantically rich textual prototypes by collecting descriptions from a large language model and verifying validity using remote sensing image features. The student module integrates lightweight and learnable prompts into both vision and language encoders, guided by the teacher to align embeddings and their cross-modal relationships. Once trained, the student operates independently during inference. Experiments on six optical remote sensing benchmarks show that AVION improves few-shot classification and base-class accuracy without degrading generalization to novel categories. It also enhances mean recall for cross-modal retrieval, with minimal additional trainable parameters. Code is publicly available at <https://github.com/yuhu990424/AVION>.

1. Introduction

Domain-specific vision–language models (VLMs) adapt rich knowledge of general-purpose foundation models to specific applications [2, 15, 35]. For example, RemoteCLIP [25] and GeoRSCLIP [41] have achieved state-of-the-art performance in remote sensing (RS) after extensive training. However, it remains a significant challenge to efficiently adapt these large-scale foundation models to new scenarios. Fully fine-

*Both authors contributed equally to this research.

†Corresponding authors.

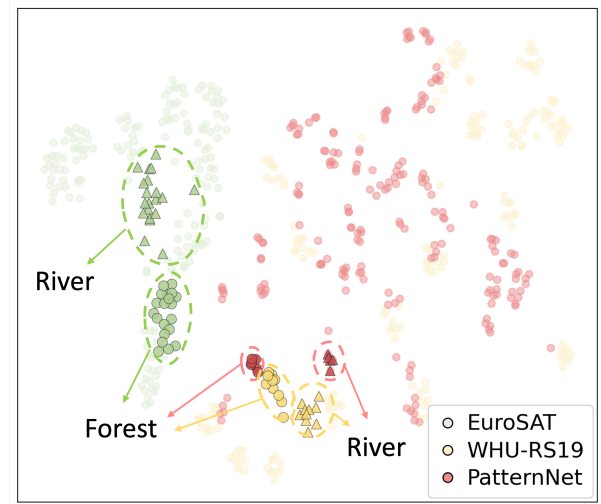


Figure 1. **The t-SNE visualization of visual embeddings from different datasets.** The same class demonstrates large variations across datasets. However, only class names are provided in the datasets, which limits multimodal alignment.

tuning the entire backbone is an ideal option to boost the performance on new tasks, but it is computationally expensive and slow. This approach is often infeasible in real-world scenarios that demand rapid deployment while having only scarce labels and limited computational resources [12, 40].

Parameter-efficient fine-tuning (PEFT) emerges as a lightweight adaptation solution [20, 43]. These methods only update a small set of parameters, leaving the backbone of foundation models frozen. While efficient, existing PEFT methods remain sub-optimal for RS. As illustrated in Fig. 1, the same category can have disparate visual appearances across different datasets. However, the images are only paired with the class name, which cannot effectively capture such visual variances. PEFT methods like CoOp [43] learn new tasks from simple templates (*e.g.*, a

photo of [CLASS]). As a result, the text encoder cannot adequately describe the diverse appearance patterns in RS data. We denote this limitation as *semantic poverty*. Such a disconnection between labels and semantics also makes generalization to novel classes challenging.

Moreover, many PEFT methods primarily update the text encoder while freezing the visual encoder. We argue that this design obscures models from capturing scale variation (e.g., large spatial context and subtle textures) and heterogeneity across sources in RS imagery. We refer to this limitation as *visual rigidity*. Although PEFT can also act on the vision side through visual prompting [19] and lightweight adapters [13], they still struggle to capture RS-specific visual features without proper guidance from the textual side.

To this end, we introduce Aerial Vision–Language Instruction (**AVION**), a knowledge distillation framework that addresses the above issues. A frozen large teacher model is employed to distill knowledge into a lightweight student model that is later used for inference. To tackle the *semantic poverty*, we use a large language model (LLM) to generate semantically rich descriptions for each class. The teacher model then aggregates these descriptions into a robust textual prototype based on its similarity with the visual embeddings of the corresponding class. This prototype contains much richer information compared with the class name alone. For *visual rigidity*, we inject learnable prompts to the visual side like VPT [19]. These prompts give the visual encoder flexibility to handle visual variations (e.g., oblique views) in the RS scenarios.

Then, we apply distillation on the visual embeddings, textual embeddings, and their similarity logits simultaneously. This tri-aspect distillation helps the student acquire the visual and textual understandings, as well as the multimodal alignment structure constructed by the teacher model. The learnable prompts for both vision and text encoders allow the student model to accumulate rich knowledge on diverse RS imagery, guided by robust textual prototypes. This flexibility maintains the generalization to unseen data. As shown in Tab. 2, AVION is the only method among state-of-the-art approaches that yields higher base-to-novel accuracy than the GeoRSCLIP baseline.

Our contributions are summarized as follows:

- We identify and analyze two critical limitations of previous PEFT methods for remote sensing imagery: semantic poverty and visual rigidity.
- We propose AVION, a knowledge distillation framework that addresses both limitations with semantically rich textual prototypes and multimodal prompt tuning for both visual and text encoders.
- With a tri-aspect alignment, AVION consistently surpasses other state-of-the-art PEFT methods in few-shot classification, base-to-novel generalization, and frozen-gallery retrieval settings.

2. Related Work

2.1. Vision-Language Models

VLMs align images and text in a shared embedding space and deliver strong zero-shot classification and cross-modal retrieval performances. Contrastive Language-Image Pre-training (CLIP) models train an image and a text encoder in a contrastive fashion [17, 27]. Subsequent advances have refined objectives [30, 39], introduced fine-grained interactions [34], or explored efficient transfer recipes [8, 38]. Other architectures have explored generative/fusion modeling [22, 36] or incorporating LLMs via lightweight bridges (e.g., BLIP-2 [23]).

2.2. Parameter-Efficient Adaptation of VLMs

The heavy foundation models motivate PEFT methods. Among these, prompt learning has emerged as a prominent approach. Text-side prompting (e.g., CoOp [43], Co-CoOp [42]) optimizes learnable context tokens, while vision-side prompting (VPT [19]) inserts prompts into ViT layers. Multi-modal prompting (MaPLe [20]) introduces paired prompts for both encoders. Beyond prompting, non-prompt adapters (e.g., CLIP-Adapter [12], Tip-Adapter [40]) attach lightweight heads or training-free caches. MMRL injects a learnable modality-agnostic representation space into higher layers to balance specialization and generalization [13]. PromptKD uses unlabeled images for logit-based distillation from a CLIP teacher to learnable prompts [24]. Prompt-CAM uses PEFT to reveal interpretable traits [9]. While efficient, these PEFT methods are sub-optimal in aligning diverse visual appearances with their class names in the RS scenario. AVION tackles this challenge via introducing semantically rich textual prototypes and prompt tuning for both vision and text encoders.

2.3. VLM Application in Remote Sensing

Remote sensing (RS) images present a significant visual domain gap compared to general-purpose web data. Unlike ground-level photos, RS images are captured from top-down perspectives, with significant variations in object scale and resolution. The progress of the VLM application has followed two fronts. The first front builds RS-specific foundation models. Works like RemoteCLIP [25], RS5M/GeoRSCLIP [41], and LRSCLIP [6] build large-scale RS datasets to train domain-specific models. Others align images directly with geographic coordinates (e.g., GeoCLIP [3], SatCLIP [21]). The second front focuses on parameter-efficient RS adaptation. For classification, APLeNet [28] generates image-conditioned visual prompt tokens by fusing multi-scale content features with domain style information. MVP [45] integrates visual prompting into a meta-learning framework. RotCLIP [29] augments CLIP with a lightweight Rot-Adapter and dual textual prompts. RSPrompter [4] and

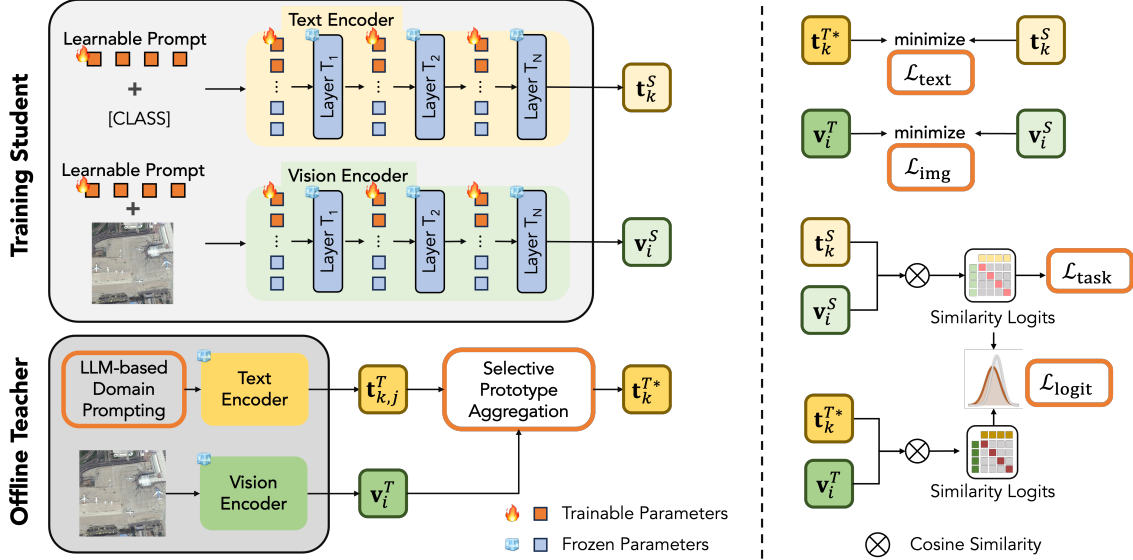


Figure 2. **Overview of AVION. Upper-left (Training Student).** Learnable prompt tokens are injected into the text and vision encoders. The student outputs embeddings: \mathbf{t}_k^S (student text embedding for class k) and \mathbf{v}_i^S (visual embedding for image i). **Bottom-left (Offline Teacher).** *LLM-based Domain Prompting* generates multiple class-aware descriptions, which are encoded into $\mathbf{t}_{k,j}^T$. *Selective Prototype Aggregation* verifies these candidates using teacher visual embeddings \mathbf{v}_i^T and aggregates them into an RS-aware text prototype \mathbf{t}_k^{T*} . **Right (Training Objectives).** Tri-aspect alignment: (i) *textual alignment* $\mathcal{L}_{\text{text}}$ maximizes the cosine similarity between \mathbf{t}_k^S and \mathbf{t}_k^{T*} ; (ii) *visual alignment* \mathcal{L}_{img} aligns \mathbf{v}_i^S with \mathbf{v}_i^T ; (iii) *similarity logit alignment* $\mathcal{L}_{\text{logit}}$ matches teacher logits $s_{i,k}^T = (\mathbf{v}_i^T)^\top \mathbf{t}_k^{T*}$ and student logits $s_{i,k}^S = (\mathbf{v}_i^S)^\top \mathbf{t}_k^S$ via temperature-scaled KL. A standard task loss $\mathcal{L}_{\text{task}}$ (cross-entropy) is applied on the student.

RSRefSeg [5] learn prompts for segmentation. PefCD [11] plugs LoRA and Adapter modules into Siamese backbones for change detection. Compared with other explorations, AVION focuses on the intrinsic visual variation of RS imagery. The distillation improves adaptation results under realistic settings while retaining efficiency.

3. Methodology

Compared with general web images, remote sensing (RS) imagery poses unique challenges [10, 16]. First, RS images present a large gap from general images, which stems from the top-down perspective. Second, within RS domains, the same semantic category can have drastically different visual appearances due to the variations of regions, seasons, sensor types, and resolutions. These challenges make existing PEFT methods inadequate for adapting foundation models to new scenarios. In this work, we propose an AVION distillation framework for more robust adaptation performance without sacrificing efficiency. An overview of the proposed AVION framework is illustrated in Fig. 2.

3.1. Preliminary

Let $\mathcal{X} = \{(\mathbf{x}_i, y_i)\}_{i=1}^N$ be the training set, where the label $y_i \in \mathcal{Y} = \{1, \dots, C\}$. We employ a large teacher model in the training process to provide distillation supervision. Learnable deep prompts are injected into a student model whose backbone parameters are frozen [18]. We denote the

visual and textual embeddings encoded by the teacher model as \mathbf{v}^T and \mathbf{t}^T , respectively. Similarly, the student’s visual and textual embeddings are denoted as \mathbf{v}^S and \mathbf{t}^S . Logit $s_{i,k}$ represents the similarity between visual embedding \mathbf{v}_i and textual embedding \mathbf{t}_k . We present a summary of all the symbols and hyperparameter settings in Appendix B.

As discussed, adapting VLMs to RS is challenged by two critical limitations: (1) *semantic poverty*, as simple class names fail to capture fine-grained visual distinctions; (2) *visual rigidity*, as the frozen visual encoder struggles with RS-specific features. There is a necessity for a framework that enriches textual supervision while enhancing visual adaptability to mitigate the gap of RS-tailored adaptation.

Therefore, we propose to design a distillation framework that efficiently adapts RS foundation models to new application scenarios. Specifically, we propose to enhance the textual prototype to incorporate richer semantic information as distillation supervision. Moreover, the proposed AVION framework aligns both embeddings and similarity logits during distillation.

3.2. Textual Prototype Enhancement

The teacher model encodes images and text labels as distillation supervisions for the student model. Compared with the visual embeddings conditioned on different images, the adopted RS datasets often only provide the class name without detailed descriptions. Therefore, the textual embeddings

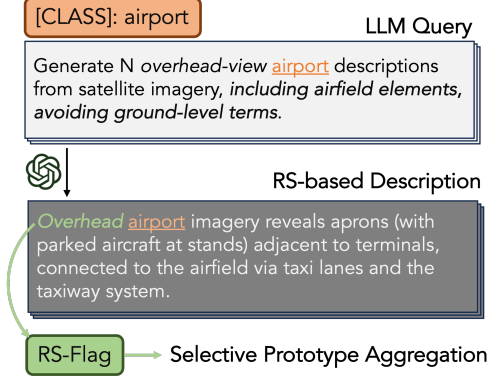


Figure 3. **LLM-based Domain Prompting.** Given a class k , an RS-aware query asks the LLM to produce aerial-view descriptions. RS-Flag is used to examine whether the description contains RS-related tokens.

can be regarded as class-specific prototypes. The corresponding visual embeddings are optimized toward the textual prototype during distillation. It also indicates that for a dataset with C classes, it will also have C different textual prototypes. As aforementioned, the class names alone cannot provide sufficient information for the intrinsic visual variations across different RS scenarios. Thus, we propose incorporating rich knowledge of large language models (LLMs) to generate descriptions for RS classes.

LLM-based domain prompting. Given a class $k \in \mathcal{Y}$, we prompt LLM to generate the corresponding descriptions in the context of RS. As shown in Fig. 3, the generated descriptions largely improve the semantic richness of the textual supervision. The detailed prompt and concrete examples of these generated candidates are presented in Appendix C.

While presenting rich semantic information, LLMs may hallucinate non-visual or non-RS-related descriptions. The textual information might not be grounded in the images as well. Therefore, it is critical to verify the validity of these descriptions based on images in each dataset. We attach an RS-Flag to each description based on the following rules: the description should contain RS-related words and exclude RS-negative words; the description should be within a proper length; the description should include class-specific cues. Details of RS-Flag are in Appendix D.

Selective prototype aggregation. To verify the LLM candidates, we first cache the teacher visual embeddings $\mathbf{v}_{k,i}^T$ of class k and obtain the visual prototype $\hat{\mathbf{v}}_k^T$ by:

$$\hat{\mathbf{v}}_k^T = \frac{1}{|\mathcal{B}_k|} \sum_{i \in \mathcal{B}_k} \mathbf{v}_{k,i}^T, \quad (1)$$

where \mathcal{B}_k is the sample set of the class k .

LLM candidates may include ground-view phrases or off-topic wording. As shown in Fig. 4, visual prototypes are used to *score* these candidates. We calculate the similarity

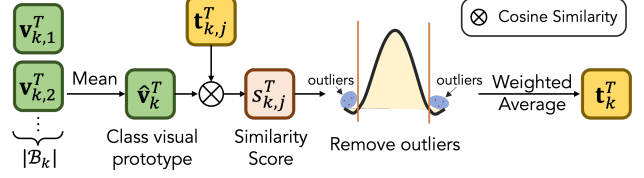


Figure 4. **Selective Prototype Aggregation.** For each class k , teacher image embeddings $\{\mathbf{v}_{k,i}^T\}_{i \in \mathcal{B}_k}$ are averaged to form the visual prototype $\hat{\mathbf{v}}_k^T$. Each LLM-generated description is encoded to a teacher text embedding $\mathbf{t}_{k,j}$ and scored by cosine similarity $s_{k,j} = (\hat{\mathbf{v}}_k^T)^\top \mathbf{t}_{k,j}^T$. A median/MAD threshold $\pm \zeta_s$ removes outlier candidates. The remaining embeddings are combined with softmax-normalized weights (over kept j) to obtain the class textual prototype \mathbf{t}_k^{T*} .

between the textual embedding $\mathbf{t}_{k,j}^T$ of each candidate description for class k and the corresponding visual prototype:

$$s_{k,j} = (\hat{\mathbf{v}}_k^T)^\top \mathbf{t}_{k,j}^T. \quad (2)$$

Next, we remove outlying or generic candidates using a median/MAD-based robust z -score (closed form in Appendix D, Eq. 9). We denote the kept index set by \mathcal{J}_k . The kept candidates are then aggregated based on the RS-Flag acquired from the last step to obtain the final prototype \mathbf{t}_k^{T*} :

$$w_{k,j} \propto \exp(\beta s_{k,j} + \gamma \text{RS-Flag}_{k,j}), \quad j \in \mathcal{J}_k, \quad (3)$$

$$\mathbf{t}_k^{T*} = \text{norm} \left(\sum_{j \in \mathcal{J}_k} \frac{w_{k,j}}{\sum_{j' \in \mathcal{J}_k} w_{k,j'}} \mathbf{t}_{k,j}^T \right), \quad (4)$$

where $\text{RS-Flag}_{k,j} \in \{0, 1\}$.

This aggregation process is analogous to a parameter-free cross-attention mechanism. The class visual prototype ($\hat{\mathbf{v}}_k^T$) acts as the *query*, and the candidate text embeddings ($\mathbf{t}_{k,j}^T$) serve as both *keys* and *values*. The RS-Flag prior is then added as a *calibration* to the scores before the softmax-like normalization (Eq. 3). Then, the weights $w_{k,j}$ are normalized over the kept set \mathcal{J}_k . In such a way, we obtain the textual prototype \mathbf{t}_k^{T*} for class k generated by the teacher model. This prototype contains richer semantic information compared with solely the class name, and also corresponds to the visual features in the target adaptation scenario.

3.3. Tri-Aspect Alignment

After acquiring the visual and textual embeddings of the teacher model, as illustrated in Fig. 2, we apply distillation training to update the learnable prompts in the student model. First, we apply the task supervision $\mathcal{L}_{\text{task}}$ (cross-entropy in this classification task) to ensure that the student model achieves the desired task performance. Additionally, we apply three complementary alignment losses to ensure comprehensive knowledge transfer:

- **Visual alignment** (\mathcal{L}_{img}): We encourage the student’s visual embeddings \mathbf{v}_i^S to mimic the teacher’s \mathbf{v}_i^T :

$$\mathcal{L}_{\text{img}} = \frac{1}{|\mathcal{B}|} \sum_{i \in \mathcal{B}} (1 - (\mathbf{v}_i^S)^\top \mathbf{v}_i^T), \quad (5)$$

where \mathcal{B} is the current mini-batch. By injecting learnable prompts into the vision side, we aim to address the *visual rigidity* of previous methods. This objective guides the student to “see” RS-specific geometric patterns (e.g., oblique views) as the teacher model does.

- **Textual alignment** ($\mathcal{L}_{\text{text}}$): This loss provides the primary supervision signal for the student’s learnable text prompts. Its effect is to align the student’s text embedding (\mathbf{t}_k^S) with the high-quality, visually-verified teacher prototypes (\mathbf{t}_k^{T*}):

$$\mathcal{L}_{\text{text}} = \frac{1}{C} \sum_{k=1}^C (1 - (\mathbf{t}_k^S)^\top \mathbf{t}_k^{T*}). \quad (6)$$

By minimizing the cosine distance, the student can produce semantic representations that mimic the rich, LLM-guided knowledge captured by the teacher, thereby combating *semantic poverty*.

- **Similarity logit alignment** ($\mathcal{L}_{\text{logit}}$): This loss aligns the student’s predictive output distribution with the teacher’s (Eq. 7). In contrast to $\mathcal{L}_{\text{task}}$, which uses a one-hot vector representing only the single ground-truth class, this objective provides a more informative supervisory signal. The effect is that the student is trained to replicate the teacher’s *entire probability distribution* over all classes:

$$\mathcal{L}_{\text{logit}} = \frac{1}{|\mathcal{B}|} \sum_{i \in \mathcal{B}} \tau^2 \text{KL}(\sigma(\mathbf{s}_{i,\cdot}^{(T)}/\tau) \parallel \sigma(\mathbf{s}_{i,\cdot}^{(S)}/\tau)). \quad (7)$$

This distribution contains rich, implicit information about inter-class relationships, capturing subtle similarities that are lost in the one-hot target.

The overall objective is a weighted sum:

$$\mathcal{L} = \mathcal{L}_{\text{task}} + \lambda_{\text{img}} \mathcal{L}_{\text{img}} + \lambda_{\text{text}} \mathcal{L}_{\text{text}} + \lambda_{\text{logit}} \mathcal{L}_{\text{logit}}. \quad (8)$$

The teacher is only used during training. We present the complexity analysis in Appendix F and detailed hyper-parameter settings in Appendix B.

4. Experiments

4.1. Experimental Setup

We evaluate AVION on standard RS benchmarks for few-shot classification, base-to-novel generalization, and cross-modal retrieval.

Few-shot learning. To assess the performance of AVION under limited supervision, which is common in remote sensing, we evaluate few-shot classification under different settings of

labeled examples per class ($K \in \{1, 2, 4, 8, 16\}$). To ensure a fair comparison, we fix identical per-class samples across all runs for each method and K .

Base-to-novel generalization. Each dataset is split into disjoint base/novel classes. Models are trained on base classes with 16-shot supervision and evaluated on both sets. We report the harmonic mean (HM) following prompt-learning practice [13, 20, 42, 43]. To prevent information leakage from novel classes, the teacher builds prototypes only for base classes. Please refer to Appendix E for the masking mechanism.

Cross-modal retrieval. To perform cross-modal retrieval, we extract image and text representations. These are ℓ_2 -normalized, and we retrieve the most similar samples using cosine similarity (the normalized dot product). We report retrieval recall at R@1, R@5, and R@10 for both image-to-text (I→T) and text-to-image (T→I) directions. We also report the mean recall (mR), the average of all six values.

Datasets. For classification (few-shot and base-to-novel), we use AID [32], RESISC-45 [7], EuroSAT [14], WHURS19 [31], PatternNet [44], and UCMerced [33], covering diverse spatial resolutions, class counts (19–45), and scene complexities. For cross-modal retrieval, we use RSITMD [37] and RSICD [26].

Implementation details. Unless noted, the student backbone is GeORSCLIP (ViT-B/32) [41] and the frozen teacher is GeORSCLIP (ViT-H/14) [41]. All teacher-side visual prototypes and textual prototypes generated by selective prototype aggregation are prepared offline and used only during training. Specifically, we employ the Gemini 2.5 Flash API for LLM-based domain prompting to generate up to 50 class-specific descriptions per class. For training, we use AdamW with a learning rate of 5×10^{-4} and a batch size of 4. Few-shot runs train for 100 epochs; base-to-novel and retrieval for 50 epochs. For the distillation objective, we set the final weights to $\lambda_{\text{img}}=0.5$, $\lambda_{\text{text}}=0.5$, and $\lambda_{\text{logit}}=1.0$, using a 30% linear warm-up for the λ_{logit} term to ensure stable convergence. The distillation temperature τ is fixed at 2. All hyperparameters were selected on a validation split of the AID dataset and then fixed for all other datasets and tasks. We provide a detailed justification for these choices, including sensitivity analysis, in Appendix G. All experiments were run on a single NVIDIA L4 GPU (24 GB).

4.2. Few-shot Evaluation

We compare AVION with two groups of baselines. (1) Zero-shot VLMs: CLIP [27], RemoteCLIP [25], and GeORSCLIP [41], all evaluated in the zero-shot mode. (2) Parameter-efficient fine-tuning (PEFT): (a) prompt-learning methods CoOp [43], CoCoOp [42], MaPLe [20], PromptKD [24], and APPLeNet [28]; (b) a representation-token based method MMRL [13]. To ensure fairness, all PEFT

Table 1. Few-shot classification against state-of-the-art methods. The table presents the average classification accuracy (%) over 6 datasets. The best-performing result for each K -shot setting is in **bold**, and the runner-up is underlined.

Method	1-shot	2-shot	4-shot	8-shot	16-shot
Zero-shot Methods					
CLIP [27]			63.24		
RemoteCLIP [25]			<u>72.92</u>		
GeoRSCLIP [41]			72.95		
PEFT Methods					
CoOp [43]	69.98	78.95	84.52	87.57	90.24
CoCoOp [42]	70.27	80.56	85.74	88.93	91.41
MMRL [13]	70.57	79.47	84.66	87.48	90.45
MaPLe [20]	65.60	76.69	82.48	88.33	90.73
PromptKD [24]	69.91	79.64	85.02	88.27	90.86
APPLeNet [28]	<u>74.27</u>	<u>81.79</u>	<u>86.40</u>	<u>89.20</u>	<u>91.61</u>
AVION (Ours)	74.27	81.86	88.31	91.85	93.69

Table 2. Average base-to-novel results (%) across all 6 datasets (ViT-B/32 student). We report Base, Novel, and HM.

Method	Base	Novel	HM
GeoRSCLIP [41]	78.10	<u>79.75</u>	78.81
CoOp [43]	91.17	69.52	78.88
CoCoOp [42]	91.85	70.69	80.06
MMRL [13]	93.75	73.69	82.76
MaPLe [20]	92.87	74.66	82.90
PromptKD [24]	93.67	76.58	<u>84.20</u>
APPLeNet [28]	<u>93.84</u>	75.75	83.84
AVION (Ours)	95.64	79.94	87.05

baselines are implemented on the same CLIP-like backbone GeoRSCLIP, keeping the image/text encoders frozen while training only method-specific lightweight parameters.

As shown in Tab. 1, AVION matches or exceeds other methods across all shot levels. At 1-shot, it ties the top method (74.27%), and its performance margin over the runner-up progressively widens with more training samples, peaking at +2.65 pp at 8-shot. We attribute this high data efficiency to learnable visual prompts and semantically rich textual prototypes generated by the teacher. The textual prototypes are then effectively incorporated via our tri-aspect alignment objective, capturing more supervision signals. Even if the adopted initialization (GeoRSCLIP) already achieves strong zero-shot performance [41], with RS-specific optimizations in both teacher and student models, our method yields even more significant improvements.

4.3. Base-to-Novel Generalization

The base-to-novel setting evaluates the adaptation to base classes and the generalization to novel classes after fine-tuning. As shown in Tab. 2, with a strong initialization (GeoRSCLIP), all previous methods achieve higher performances on base classes. However, the adaptation also

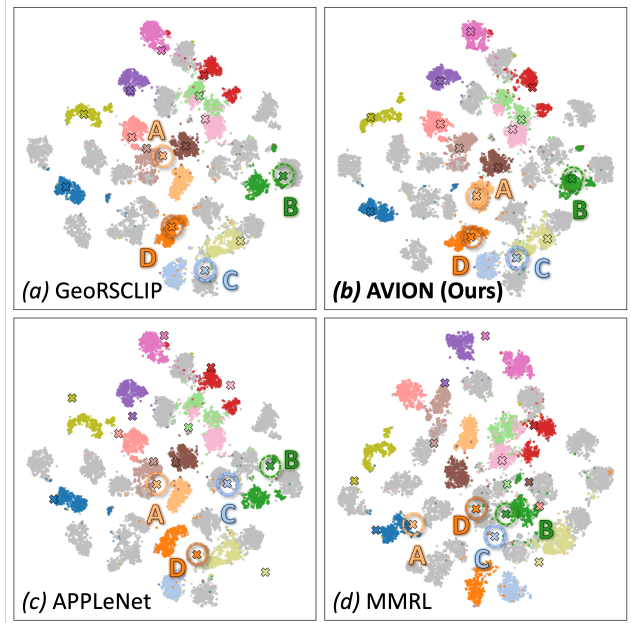


Figure 5. t-SNE of base-to-novel visual and text embeddings on RESISC-45. (a) GeoRSCLIP [41] (b) AVION (ours) (c) APPLeNet [28] (d) MMRL [13]. Gray dots represent the visual embedding of *base classes*. Colored dots represent the *visual embedding of novel classes* with each color standing for a class. Colored crosses represent the *text embedding of novel classes* for their class names. A, B, C, and D are four classes.

leads to degraded performance on novel classes. In our comparison, AVION is the only method that surpasses GeoRSCLIP [41] in novel-class performance. Meanwhile, AVION also achieves the best performance on base classes, surpassing the runner-up by +1.80pp.

We present the t-SNE visualization of visual and text embeddings for both base and novel classes in Fig. 5. Gray clusters correspond to base classes, while colored clusters denote novel classes (each color indicates a different class). Colored crosses represent the text embedding of class names for the corresponding colored classes. A, B, C, and D are four representative classes. We highlight their text embeddings with dashed circles. Overall, AVION shows slightly better (e.g., classes A and B) or on-par multimodal alignment on novel classes compared with GeoRSCLIP [41]. It corresponds to the quantitative results in Tab. 2. By contrast, the other two methods, APPLeNet [28] and MMRL [13], illustrate misalignment between text and visual embeddings. APPLeNet freezes the visual encoder and updates only the text encoder. While the visual embedding distribution remains consistent with GeoRSCLIP, the text embeddings on these unseen classes shift after tuning. MMRL opens both encoders for training, but without semantically rich text prototypes as guidance, the multimodal gap becomes even larger for unseen classes.

Table 3. Cross-modal retrieval ($\mathbf{R@K}$, %) on RSITMD [37] and RSICD [26] (ViT-B/32 student; protocol details in Sec. 4.1). \mathbf{mR} is the macro-average over $\{T \rightarrow I, I \rightarrow T\} \times \{1, 5, 10\}$. Δ is relative to GeoRSCLIP. Our method (AVION) is lightweight, updating only prompts/heads; see Appendix F for a full efficiency analysis.

Testing Dataset	Training Dataset	Method	Image \rightarrow Text			Text \rightarrow Image			mR
			R@1	R@5	R@10	R@1	R@5	R@10	
RSITMD [37]	RSITMD	ML Retrieval [1]	19.09	40.26	54.42	17.61	49.73	60.59	41.38
	RET-3	CLIP [27]	23.67	50.00	63.27	22.61	55.27	69.87	47.63
	RET-3 + DET-10 + SEG-4	RemoteCLIP [25]	27.88	50.66	65.71	22.17	56.46	67.41	49.38
	RSITMD + RSICD	GeoRSCLIP-FT [41]	32.30	53.32	67.92	25.04	57.88	74.38	51.81
	RSITMD + RSICD	AVION (Ours)	33.17	54.46	69.18	26.09	59.22	75.41	52.92
RSICD [26]	RSICD	ML Retrieval [1]	10.70	29.64	41.53	9.14	29.98	44.59	27.43
	RET-3	CLIP [27]	17.94	35.94	51.04	13.89	35.15	50.08	33.98
	RET-3 + DET-10 + SEG-4	RemoteCLIP [25]	17.02	39.97	51.51	13.73	34.71	48.28	35.26
	RSITMD + RSICD	GeoRSCLIP-FT [41]	21.13	41.72	55.63	15.59	41.19	57.99	38.87
	RSITMD + RSICD	AVION (Ours)	22.01	42.37	56.42	16.24	42.58	59.21	39.80
Δ vs. GeoRSCLIP-FT (mR)			RSITMD: +1.11			RSICD: +0.93			

Table 4. **Configurations for our incremental ablation study.** Each configuration builds upon the previous one and culminates in the full system (B7).

ID	Configuration Description	ID	Configuration Description
B0	Shallow text-only prompt (CoOp-style), $\mathcal{L}_{\text{task}}$ only.	B4	Replace manual prototypes with LLM-generated ones.
B1	+ Deep prompt tuning.	B5	+ <i>Selective prototype aggregation</i> (vision-guided).
B2	+ Representation alignment (\mathcal{L}_{img}).	B6	+ Behavioral alignment ($\mathcal{L}_{\text{logit}}$) in a single-stage schedule.
B3	+ Semantic alignment ($\mathcal{L}_{\text{text}}$) with manual textual prototypes.	B7	Final Model: 30% warm-up (Sec. 4.1).

The teacher textual prototypes in AVION integrate rich knowledge from LLMs into the distillation process. Through verification with dataset-specific visual prototypes, AVION accurately aligns various visual appearances with their corresponding labels and descriptions. The external knowledge, in addition to class names, facilitates a comprehensive understanding of base classes, which further promotes the generalization to novel classes.

4.4. Cross-modal Retrieval

We evaluate cross-modal retrieval using a deployment-oriented protocol. To simulate scenarios where the gallery is fixed, gallery embeddings are pre-computed and are not re-encoded during adaptation. Concretely, AVION uses a lightweight prompt learning approach, which requires updating only a minimal set of parameters (well below 1% of the backbone) and no gallery recomputation. This resource-efficient design is detailed in Appendix F.

As shown in Tab. 3, AVION attains the best mR across both directions with lightweight adaptation on RSITMD and RSICD. Compared with GeoRSCLIP-FT, which opens all the parameters for tuning, AVION improves mR by +1.11 pp (RSITMD) and +0.93 pp (RSICD). This indicates the computational efficiency of our framework. When the trainable parameters are fewer, we introduce additional rich knowl-

edge from LLMs to promote the understanding of these RS classes. The results demonstrate that this semantically richer supervision and our tri-aspect alignment objective are more effective than naive full fine-tuning.

4.5. Ablation Study

Incremental ablation analysis. We conduct an incremental ablation study to quantify the contribution of each component of AVION. Starting from a minimal prompt-only baseline, we enable deep prompt tuning, textual prototype enhancement, and the tri-aspect alignment objective ($\mathcal{L}_{\text{img}}, \mathcal{L}_{\text{text}}, \mathcal{L}_{\text{logit}}$). Eight configurations (B0–B7) and their results are listed in Tab. 4 and Tab. 5, respectively. All runs share identical training budgets, datasets, and evaluation protocols. To avoid leakage in the base-to-novel protocol, the offline teacher is used only during training, and its guidance (textual prototypes and distillation targets) is restricted to base classes with masked re-normalization. More details are presented in Appendix E.

Injecting deep prompts (B1) alone improves the base-class accuracy, but also leads to a -16.01 pp degradation on novel classes. When gradually adding more training samples, the improvement of deep prompts becomes marginal, indicating unstable effects.

Adding visual alignment (B2) acts as an effective reg-

Table 5. **Main ablation results for classification.** We report Base, Novel, and Harmonic Mean (HM) accuracy. Metrics are averaged over six datasets.

ID	Base	Novel	HM	K-shot				
				1	2	4	8	16
B0	91.17	69.52	78.88	69.98	78.95	84.52	87.57	90.24
B1	93.52	53.51	66.71	66.95	84.68	84.61	87.34	91.25
B2	89.74	61.15	72.74	70.21	82.99	85.31	89.65	91.51
B3	91.21	68.63	78.34	71.98	83.72	85.90	90.43	92.18
B4	91.03	74.08	81.67	72.15	84.71	87.43	91.89	92.14
B5	91.71	75.87	83.05	72.52	85.06	87.91	92.53	92.65
B6	94.82	79.14	86.26	73.71	85.34	89.28	92.95	93.17
B7	95.64	79.94	87.05	74.27	81.86	88.31	91.85	93.69

ularizer, partially reversing the generalization degradation (HM +6.03 pp). Except for the 2-shot case, B2 outperforms B0 across all few-shot configurations. This supports the necessity of introducing the visual alignment \mathcal{L}_{img} .

Introducing our enhanced textual prototypes at this stage delivers the largest cumulative HM improvement (+10.31 pp from B2 to B5). This trajectory is paralleled in the few-shot domain, which sees cumulative gains from B2 to B5 of +2.31 pp (1-shot) and +1.14 pp (16-shot). These results are consistent with the hypothesis that high-quality, visually grounded semantics are pivotal for both generalization and data efficiency.

Finally, adding similarity logit alignment (\mathcal{L}_{logit} , B6) and an optimized warm-up schedule (B7) yields a further HM gain (+4.00 pp from B5 to B7). This final optimization pushes HM, 1-shot, and 16-shot to their peak values. Overall, B7 provides the best overall performance, particularly in generalization (HM) and extreme few-shot scenarios.

Ablating the teacher text-prototype pipeline. We fix the model architecture and training objectives for all settings, varying only prototype sources and aggregation in Tab. 6. Handcrafted multi-templates (P1) serve as a baseline (79.91 HM). Switching to domain-constrained LLM candidates with simple averaging (P3) already improves this to 81.70 HM. This highlights the importance of the additional knowledge introduced by LLMs. *Selective prototype aggregation* (P6) further boosts the score to 83.05 HM. This +1.35 pp gain (P6 vs. P3) isolates the benefit of our aggregation over a simple mean. The value of its *visual* guidance is also supported by P5 outperforming a text-only selector (P4, 82.05 HM). We also demonstrate the result of selecting a random subset from candidates (P5), which results in a score of 80.31 HM. Notably, random selection performs even worse than averaging all unconstrained candidates (P2, 80.85 HM). The contrast further supports that P6’s gains stem from its vision-guided selection criteria.

Backbone variants (CLIP family). We compare AVION’s performance using three different ViT-B/32 backbones:

Table 6. **Teacher text-prototype ablation (P0–P6).** All settings use the same objectives, with different prototype sources and aggregation. HM averaged over the same datasets/seeds.

ID	Prototype Source	Aggregation	RS-Flag	HM (%)
P0	Manual (single template)	none	–	79.52
P1	Manual (multi-templates)	mean	–	79.91
P2	LLM (unconstrained)	mean	no	80.85
P3	LLM (domain-constrained)	mean	yes	81.70
P4	LLM (domain-constrained)	text-only selection	yes	82.05
P5	LLM (random subset)	mean	no	80.31
P6	LLM (domain-constrained)	Selective agg.	yes	83.05

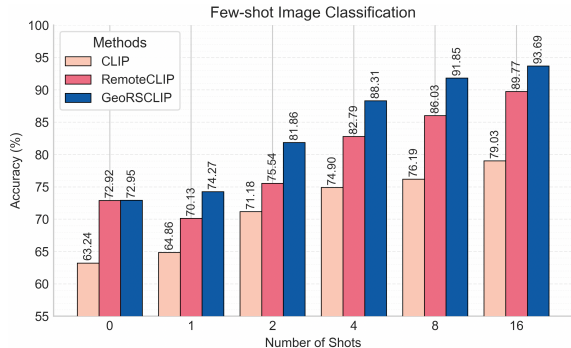


Figure 6. Few-shot classification accuracy of AVION with different CLIP-based backbones in the few-shot setting.

CLIP, RemoteCLIP, and GeoRSCLIP. The choice of backbone has a clear impact. As seen in Fig. 6, the domain-pretrained GeoRSCLIP achieves the highest accuracy across all settings, from zero-shot up to 16-shot. RemoteCLIP, which is also pre-trained for remote sensing, is the clear second-best. The general CLIP backbone performs last in all cases. This result aligns with the expectation that backbones already familiar with aerial imagery provide a stronger starting point for adaptation. We also observe that, starting from 1-shot, the performance for all variants consistently improves over the zero-shot initializations.

5. Conclusion

We addressed two challenges in adapting vision–language models to remote sensing imagery: semantic poverty in text representations and visual rigidity in feature adaptation. We proposed AVION, a knowledge distillation framework in which a frozen teacher constructs semantically rich textual prototypes from LLM-generated descriptions and remote sensing image features, and a lightweight student learns multimodal prompts for both vision and language encoders under a tri-aspect alignment objective. This design allows the student to better accommodate appearance variations in aerial scenes while preserving the alignment structure induced by the teacher. Experiments on six remote sensing benchmarks indicate that AVION can improve few-shot classification performance without degrading generalization to novel categories.

Acknowledgments

This work was supported by Mitacs through the Mitacs Accelerate Program and by TerraSense Analytics (Grant No. IT42711). It was supported in part by the U.S. National Science Foundation (OAC-2118240, HDR Institute: Imageomics).

References

- [1] Mohamad M Al Rahhal, Yakoub Bazi, Norah A Alsharif, Laila Bashmal, Naif Alajlan, and Farid Melgani. Multilingual transformer for improved text to remote sensing image retrieval. *IEEE Journal of Selected Topics in Applied Earth Observations and Remote Sensing*, 15:9115–9126, 2022. 7
- [2] Muhammad Awais, Muzammal Naseer, Salman Khan, Rao Muhammad Anwer, Hisham Cholakkal, Mubarak Shah, Ming-Hsuan Yang, and Fahad Shahbaz Khan. Foundation models defining a new era in vision: a survey and outlook. *IEEE Transactions on Pattern Analysis and Machine Intelligence*, 2025. 1
- [3] Vicente Vivanco Cepeda, Gaurav Kumar Nayak, and Mubarak Shah. Geoclip: Clip-inspired alignment between locations and images for effective worldwide geo-localization. In *NeurIPS (Workshop/Conference)*, 2023. 2
- [4] Keyan Chen, Chenyang Liu, Hao Chen, Haotian Zhang, Wenyuan Li, Zhengxia Zou, and Zhenwei Shi. Rsprompter: Learning to prompt for remote sensing instance segmentation based on visual foundation model. *IEEE Transactions on Geoscience and Remote Sensing*, 62:1–17, 2024. 2
- [5] Kyan Chen et al. Rrefseg: Text-guided referring remote sensing image segmentation with foundation models. *arXiv preprint arXiv:2501.06809*, 2025. 3
- [6] Weizhi Chen, Jingbo Chen, Yupeng Deng, and et al. Lrsclip: Aligning remote sensing images with longer text (lrs2m dataset). *arXiv:2503.19311*, 2025. 2
- [7] Gong Cheng, Junwei Han, and Xiaoqiang Lu. Remote Sensing Image Scene Classification: Benchmark and State of the Art. *Proceedings of the IEEE*, 105(10):1865–1883, 2017. Introduces NWPU-RESISC45. 5, 2, 4
- [8] Mehdi Cherti, Romain Beaumont, Ross Wightman, and et al. Reproducible scaling laws for contrastive language-image pre-training. In *CVPR*, 2023. 2
- [9] Arpita Chowdhury, Dipanjyoti Paul, Zheda Mai, Jianyang Gu, Ziheng Zhang, Kazi Sajeed Mehrab, Elizabeth G Campolongo, Daniel Rubenstein, Charles V Stewart, Anuj Karpatne, et al. Prompt-cam: Making vision transformers interpretable for fine-grained analysis. In *Proceedings of the Computer Vision and Pattern Recognition Conference*, pages 4375–4385, 2025. 2
- [10] Rajeshreddy Datla, Nazil Perveen, et al. Learning scene-vectors for remote sensing image scene classification. *Neurocomputing*, 587:127679, 2024. 3
- [11] Sijun Dong, Yuxuan Hu, LiBo Wang, Geng Chen, and Xiaoliang Meng. PeftCD: Leveraging vision foundation models with parameter-efficient fine-tuning for remote sensing change detection. *arXiv preprint arXiv:2509.09572*, 2025. 3
- [12] Peng Gao, Shijie Geng, Renrui Zhang, Teli Ma, Rongyao Fang, Yongfeng Zhang, Hongsheng Li, and Yu Qiao. Clip-adapter: Better vision-language models with feature adapters. *International Journal of Computer Vision*, 132(2):581–595, 2024. 1, 2
- [13] Yuncheng Guo and Xiaodong Gu. Mmrl: Multi-modal representation learning for vision-language models. In *Proceedings of the Computer Vision and Pattern Recognition Conference*, pages 25015–25025, 2025. 2, 5, 6, 4
- [14] Patrick Helber, Benjamin Bischke, Andreas Dengel, and Damian Borth. EuroSAT: A novel dataset and deep learning benchmark for land use and land cover classification. *IEEE Journal of Selected Topics in Applied Earth Observations and Remote Sensing*, 12(7):2217–2226, 2019. 5, 2, 4
- [15] Ziyue Huang, Hongxi Yan, Qiqi Zhan, Shuai Yang, Mingming Zhang, Chenkai Zhang, YiMing Lei, Zeming Liu, Qingjie Liu, and Yunhong Wang. A survey on remote sensing foundation models: From vision to multimodality. *arXiv preprint arXiv:2503.22081*, 2025. 1
- [16] Chunlei Huo, Keming Chen, Shuaihao Zhang, Zeyu Wang, Heyu Yan, Jing Shen, Yuyang Hong, Geqi Qi, Hongmei Fang, and Zihan Wang. When remote sensing meets foundation model: A survey and beyond. *remote sensing*, 17(2), 2025. 3
- [17] Chao Jia, Yinfei Yang, Ye Xia, and et al. Scaling up visual and vision-language representation learning with noisy text supervision. In *ICML*, 2021. 2
- [18] Menglin Jia, Luming Tang, Bor-Chun Chen, Claire Cardie, Serge Belongie, Bharath Hariharan, and Ser-Nam Lim. Visual prompt tuning, 2022. 3
- [19] Menglin Jia, Luming Tang, Bor-Chun Chen, Claire Cardie, Serge Belongie, Bharath Hariharan, and Ser-Nam Lim. Visual prompt tuning. In *Computer Vision – ECCV 2022*, pages 709–727. Springer, 2022. 2
- [20] Muhammad Uzair Khattak, Hanoona Rasheed, Muhammad Uzair Maaz, Salman Khan, Fahad Shahbaz Khan, and Ming-Hsuan Yang. Maple: Multi-modal prompt learning. In *Proceedings of the IEEE/CVF Conference on Computer Vision and Pattern Recognition (CVPR)*, pages 19113–19122, 2023. 1, 2, 5, 6, 4
- [21] Konstantin Klemmer, Esther Rolf, Caleb Robinson, Lester Mackey, and Marc Rußwurm. Satclip: Global, general-purpose location embeddings with satellite imagery. In *AAAI*, 2025. 2
- [22] Junnan Li, Ramprasaath R. Selvaraju, Akhilesh Gotmare, and et al. Align before fuse: Vision and language representation learning with momentum distillation. In *NeurIPS*, 2021. 2
- [23] Junnan Li, Dongxu Li, Silvio Savarese, and Steven C. H. Hoi. Blip-2: Bootstrapping language-image pre-training with frozen image encoders and large language models. In *ICML*, 2023. 2
- [24] Zheng Li, Xiang Li, Xinyi Fu, Xin Zhang, Weiqiang Wang, Shuo Chen, and Jian Yang. Promptkd: Unsupervised prompt distillation for vision-language models. In *Proceedings of the IEEE/CVF Conference on Computer Vision and Pattern Recognition (CVPR)*, 2024. arXiv:2403.02781. 2, 5, 6, 4
- [25] Fan Liu, Delong Chen, Zhangqingyun Guan, and et al. Remoteclip: A vision–language foundation model for remote sensing. *arXiv:2306.11029*, 2023. 1, 2, 5, 6, 7

- [26] Xiaoqiang Lu, Binqiang Wang, Xiangtao Zheng, and Xuelong Li. Exploring models and data for remote sensing image caption generation. *arXiv:1712.07835*, 2017. 5, 7
- [27] Alec Radford, Jong Wook Kim, Chris Hallacy, and et al. Learning transferable visual models from natural language supervision. In *ICML*, 2021. 2, 5, 6, 7
- [28] Mainak Singha, Ankit Jha, Bhupendra Solanki, Shirsha Bose, and Biplab Banerjee. Applenet: Visual attention parameterized prompt learning for few-shot remote sensing image generalization using clip. In *Proceedings of the IEEE/CVF Conference on Computer Vision and Pattern Recognition (CVPR) Workshops*, pages 2024–2034, 2023. 2, 5, 6, 4
- [29] Tiecheng Song, Qi Liu, Anyong Qin, and Yin Liu. Rotclip: Tuning clip with visual adapter and textual prompts for rotation robust remote sensing image classification. *Signal Processing: Image Communication*, page 117407, 2025. 2
- [30] Michael Tschannen, Alexey Gritsenko, Xiao Wang, Muhammad Ferjad Naeem, Ibrahim Alabdulmohsin, Nikhil Parthasarathy, Talfan Evans, Lucas Beyer, Ye Xia, Basil Mustafa, Olivier Hénaff, Jeremiah Harmsen, Andreas Steiner, and Xiaohua Zhai. Siglip 2: Multilingual vision-language encoders with improved semantic understanding, localization, and dense features, 2025. 2
- [31] Gui-Song Xia, Wen Yang, Julie Delon, Yann Gousseau, Hong Sun, and Henri Maître. Structural high-resolution satellite image indexing. In *ISPRS TC VII Symposium-100 Years ISPRS*, pages 298–303, 2010. 5, 2, 4
- [32] Gui-Song Xia, Jingwen Hu, Fan Hu, Baoguang Shi, Xiang Bai, Yanfei Zhong, Liangpei Zhang, and Xiaoqiang Lu. Aid: A benchmark data set for performance evaluation of aerial scene classification. *IEEE Transactions on Geoscience and Remote Sensing*, 55(7):3965–3981, 2017. 5, 2, 4
- [33] Yi Yang and Shawn Newsam. Bag-of-visual-words and spatial extensions for land-use classification. In *ACM SIGSPATIAL GIS*, 2010. UC Merced Land Use Dataset. 5, 2, 4
- [34] Lewei Yao, Runhui Huang, Lu Hou, and et al. Filip: Fine-grained interactive language-image pre-training. In *ICLR*, 2022. 2
- [35] Shukang Yin, Chaoyou Fu, Sirui Zhao, Ke Li, Xing Sun, Tong Xu, and Enhong Chen. A survey on multimodal large language models. *National Science Review*, 11(12):nwae403, 2024. 1
- [36] Jiahui Yu, Zirui Wang, Vijay Vasudevan, and et al. Coca: Contrastive captioners are image-text foundation models. *arXiv:2205.01917*, 2022. 2
- [37] Yansheng Yuan, Xintao Wang, et al. Exploring a fine-grained multiscale method for cross-modal remote sensing image retrieval. *arXiv preprint arXiv:2204.09868*, 2022. Introduces RSITMD dataset. 5, 7
- [38] Xiaohua Zhai, Xiao Wang, Basil Mustafa, and et al. Lit: Zero-shot transfer with locked-image text tuning. In *CVPR*, 2022. 2
- [39] Xiaohua Zhai, Basil Mustafa, Alexander Kolesnikov, and Lucas Beyer. Sigmoid loss for language image pre-training. *arXiv:2303.15343*, 2023. 2
- [40] Renrui Zhang, Wei Zhang, Rongyao Fang, Peng Gao, Kunchang Li, Jifeng Dai, Yu Qiao, and Hongsheng Li. Tip-adapter: Training-free adaption of clip for few-shot classification. In *Computer Vision – ECCV 2022*, pages 493–510. Springer, 2022. 1, 2
- [41] Zilun Zhang, Tiancheng Zhao, Yulong Guo, and Jianwei Yin. Rs5m and georsclip: A large scale vision-language dataset and a large vision-language model for remote sensing. *IEEE Transactions on Geoscience and Remote Sensing*, 2024. 1, 2, 5, 6, 7, 4
- [42] Kaiyang Zhou, Jingkang Yang, Chen Change Loy, and Ziwei Liu. Conditional prompt learning for vision-language models. In *Proceedings of the IEEE/CVF Conference on Computer Vision and Pattern Recognition (CVPR)*, pages 16816–16825, 2022. 2, 5, 6, 4
- [43] Kaiyang Zhou, Jingkang Yang, Chen Change Loy, and Ziwei Liu. Learning to prompt for vision-language models. *International Journal of Computer Vision*, 130:2337–2348, 2022. 1, 2, 5, 6, 4
- [44] Weixun Zhou, Shawn Newsam, Congmin Li, and Zhenfeng Shao. Patternnet: A benchmark dataset for performance evaluation of remote sensing image retrieval. *ISPRS journal of photogrammetry and remote sensing*, 145:197–209, 2018. 5, 2, 4
- [45] Junjie Zhu, Yiyang Li, Ke Yang, Naiyang Guan, Zunlin Fan, Chunping Qiu, and Xiaodong Yi. Mvp: Meta visual prompt tuning for few-shot remote sensing image scene classification. *IEEE Transactions on Geoscience and Remote Sensing*, 62: 1–13, 2024. 2

AVION: Aerial Vision–Language Instruction from Offline Teacher to Prompt-Tuned Network

Supplementary Material

This appendix is organized as follows:

- Section A reports additional quantitative results, including few-shot classification and base-to-novel generalization across six remote sensing benchmarks.
- Section B summarizes the symbols and the default or searched hyperparameter ranges used in AVION.
- Section C presents examples of our *LLM-based domain prompting* module for fine-grained remote sensing classes, comparing simple templates with richer LLM-generated descriptions.
- Section D details the selective prototype aggregation procedure, including the RS-Flag rules, MAD-based robust pruning, and pseudo-code for constructing teacher text prototypes.
- Section E describes the masking and renormalization strategy for the logit distillation loss $\mathcal{L}_{\text{logit}}$ in base-to-novel training.
- Section F analyzes the parameter count, FLOPs overhead, runtime, and memory footprint of AVION on top of a frozen GeoRSCLIP backbone.
- Section G presents a hyperparameter sensitivity analysis and our unified selection protocol shared across datasets and tasks.
- Section H provides a qualitative analysis of RS-Flag, visualizing how the calibration down-weights RS-agnostic or ground-level descriptions to mitigate hallucinations.
- Section I reports cross-dataset zero-shot transfer results to assess generalization and source-domain overfitting.
- Section J ablates the choice of offline LLM generators for domain prompting, demonstrating that AVION is robust to the specific LLM used.
- Section K extends the evaluation to broader general-domain benchmarks (ImageNet) to study scalability beyond remote sensing.

A. Additional Quantitative Results

We first provide additional few-shot classification results on six remote sensing datasets. Fig. 7 shows the K -shot performance of AVION and competing methods under $K \in \{1, 2, 4, 8, 16\}$ across **AID**, **EuroSAT**, **RESISC-45**, **UCMerced**, **WHU-RS19**, and **PatternNet**. As K increases, all methods exhibit smooth performance gains, and AVION remains competitive or superior across datasets, with particularly notable improvements on EuroSAT and UCMerced at higher shot counts. For completeness, Table 7 reports the per-dataset top-1 accuracies for each K . Overall, AVION performs on par with or better than strong prompt-learning

and parameter-efficient adaptation baselines across diverse remote sensing scenes.

We further complement these results with base-to-novel generalization experiments on the same six datasets. Table 8 summarizes the detailed Base, Novel, and harmonic-mean (HM) performance for the ViT-B/32 student model, including the difference Δ between **Ours** and the strongest competing baseline for each metric. Fig. 8 provides a radar-chart view of the HM values across the six datasets, offering a compact comparison of overall base-to-novel generalization. AVION achieves the best HM on all six datasets, improving upon the strongest baseline by +1.08 to +3.16 points while maintaining competitive Base and Novel accuracies. On some datasets (e.g., AID, EuroSAT), AVION trades a small decrease in Novel accuracy for a larger gain on Base and HM, while on the other datasets both Base and Novel improve.

B. Symbols and Default Hyperparameters

To facilitate clarity and reproducibility, Table 9 summarizes the symbols used throughout the paper, together with their definitions and the default values or hyperparameter search ranges adopted in our experiments. The table covers model components (encoders and prompts), loss-function terms (weights and temperatures), and data- or training-related parameters.

C. Examples of LLM-based Domain Prompting

To provide a concrete illustration of our *LLM-based domain prompting* module, this section presents example textual candidates generated for several fine-grained remote sensing classes.

As described in Sec. 3.2, our goal is to mitigate the *semantic poverty* of simple templates (e.g., “a photo of [CLASS]”) commonly used in prior work. Instead of relying on a single generic template, we prompt an LLM to generate multiple candidates that are both semantically richer and explicitly aware of the remote sensing imagery domain. Following the query design illustrated in Fig. 3, we use the following generic prompt template for each class [CLASS]:

“Generate N overhead-view descriptions of [CLASS] from satellite imagery, highlighting class-specific scene elements while avoiding any ground-level terms.”

This constraint encourages candidates that are appropriate

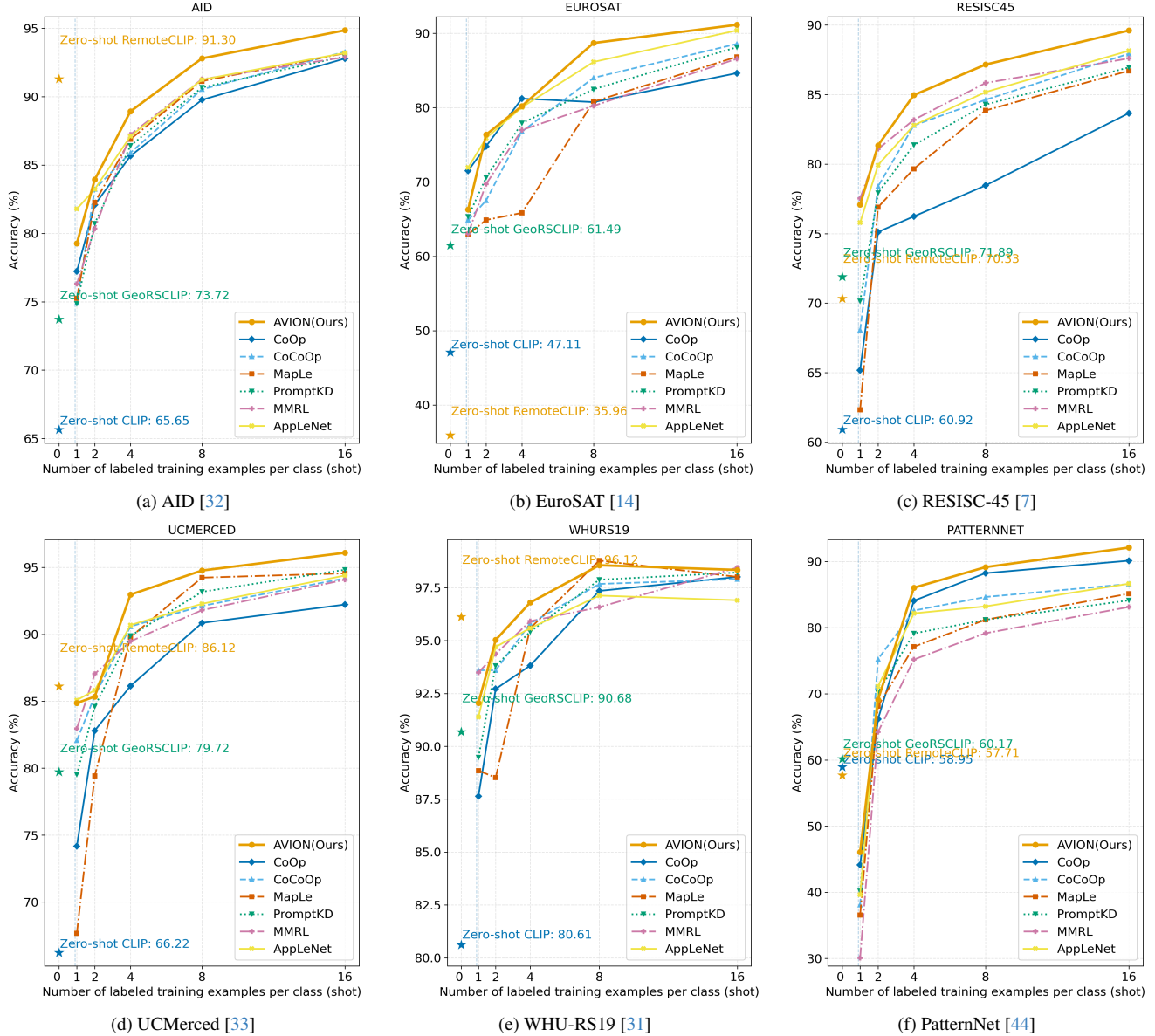


Figure 7. Few-shot classification performance (top-1 accuracy, %) across six remote sensing datasets (AID [32], EuroSAT [14], RESISC-45 [7], UCMerced [33], WHU-RS19 [31], and PatternNet [44]) for different numbers of shots $K \in \{1, 2, 4, 8, 16\}$.

for overhead perspectives and contain fine-grained, domain-specific details.

Table 10 compares standard simple templates with the candidates produced by our *LLM-based domain prompting* process. The richer descriptions provide a stronger semantic foundation for the teacher model’s prototypes, enabling our framework to better distinguish between challenging, fine-grained categories such as “industrial area” and “commercial area”.

D. Details of *Selective Prototype Aggregation*

This section provides a detailed definition of our RS-Flag prior and a step-by-step pseudo-code for the *selective prototype aggregation* process introduced in Sec. 3.2.

RS-Flag rules. The RS-Flag indicator $\text{RS-Flag}_{k,j} \in \{0, 1\}$ is set to 1 if a generated caption meets all of the following criteria, and 0 otherwise:

1. **Token constraints:** The caption must contain at least one RS-positive token and no RS-negative tokens. We use the following case-insensitive, word-boundary-matched

Table 7. Few-shot classification (top-1, %) on six remote sensing datasets. Winners are **bold**; runners-up are underlined.

Dataset	Method	1	2	4	8	16
AID	CoCoOp	74.91	83.23	85.90	90.53	<u>93.28</u>
	CoOp	77.22	82.09	85.67	89.77	92.79
	MMRL	76.30	80.35	<u>87.23</u>	<u>91.28</u>	92.89
	MaPLe	75.24	82.26	86.89	91.13	93.18
	PromptKD	74.85	80.72	86.41	90.67	92.95
	APPLeNet	81.79	<u>83.24</u>	87.11	91.24	93.20
	Ours	<u>79.27</u>	83.94	88.92	92.80	94.86
EuroSAT	CoCoOp	64.87	67.49	76.78	84.01	88.57
	CoOp	<u>71.51</u>	74.80	81.21	80.74	84.63
	MMRL	63.05	69.72	76.99	80.23	86.56
	MaPLe	62.95	64.89	65.84	80.80	86.83
	PromptKD	65.32	70.58	77.91	82.47	88.12
	APPLeNet	71.94	<u>75.89</u>	80.04	<u>86.14</u>	<u>90.38</u>
	Ours	66.29	76.36	<u>80.21</u>	88.69	91.14
RESISC-45	CoCoOp	68.06	78.40	82.78	84.62	87.94
	CoOp	65.18	75.12	76.24	78.46	83.66
	MMRL	77.53	<u>81.08</u>	<u>83.19</u>	<u>85.83</u>	87.60
	MaPLe	62.32	76.90	79.66	83.86	86.71
	PromptKD	70.14	77.92	81.37	84.28	86.95
	APPLeNet	75.79	79.94	82.79	85.18	<u>88.15</u>
	Ours	<u>77.08</u>	81.35	84.96	87.16	89.61
UCMerced	CoCoOp	82.07	85.40	90.58	92.12	94.18
	CoOp	74.18	82.80	86.14	90.85	92.22
	MMRL	82.96	87.04	89.47	91.80	94.07
	MaPLe	67.67	79.42	89.79	<u>94.23</u>	94.55
	PromptKD	79.52	84.61	89.88	93.17	<u>94.82</u>
	APPLeNet	85.08	<u>85.82</u>	<u>90.69</u>	92.28	94.39
	Ours	<u>84.87</u>	85.34	92.96	94.76	96.09
WHU-RS19	CoCoOp	93.60	93.60	95.81	97.68	97.90
	CoOp	87.64	92.72	93.82	97.35	98.01
	MMRL	<u>93.49</u>	94.37	<u>95.92</u>	96.58	98.45
	MaPLe	88.85	88.52	95.59	98.79	98.01
	PromptKD	89.47	93.81	95.42	97.88	98.22
	APPLeNet	91.39	<u>94.70</u>	95.59	97.13	96.91
	Ours	92.05	95.03	96.80	<u>98.56</u>	<u>98.34</u>
PatternNet	CoCoOp	38.09	75.23	82.58	84.63	86.59
	CoOp	<u>44.13</u>	66.18	<u>84.07</u>	<u>88.23</u>	<u>90.11</u>
	MMRL	30.09	64.23	75.18	79.15	83.11
	MaPLe	36.57	68.14	77.11	81.19	85.12
	PromptKD	40.16	70.19	79.12	81.18	84.11
	APPLeNet	39.62	<u>71.14</u>	82.16	83.21	86.63
	Ours	46.07	69.11	86.03	89.14	92.09

lists:

- **Positive:** {overhead, aerial view, satellite imagery, nadir, orthorectified, multispectral, SAR}.
- **Negative:** {street, indoor, selfie, portrait, close-up, ground level}.

2. **Length constraints:** The caption length must be between 6 and 20 words (whitespace-delimited).
3. **Content cues (optional):** The caption may optionally include class-specific cues (e.g., geometry- or infrastructure-related terms), which are captured implicitly by the LLM and the RS-Flag token lists above.

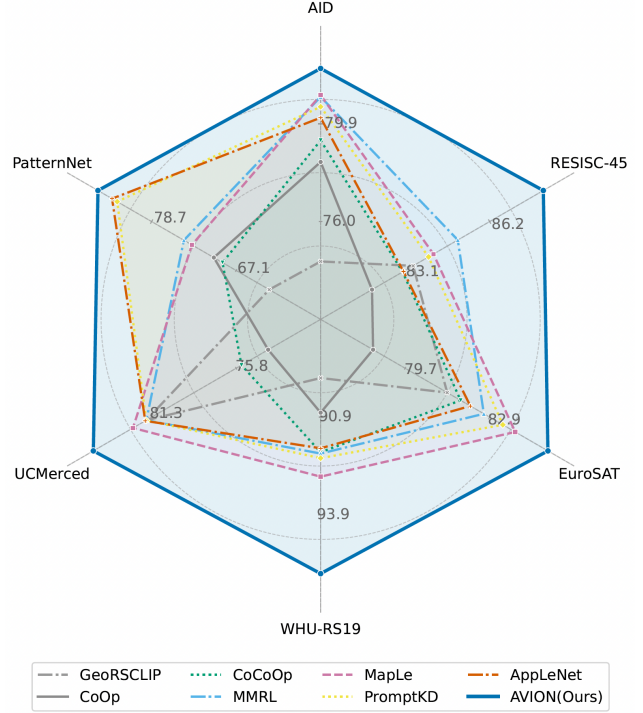


Figure 8. Base-to-novel generalization (HM, %) across six remote sensing datasets (ViT-B/32 student). The radar chart plots the harmonic mean between base and novel accuracies for AVION and competing baselines; a larger enclosed area indicates better overall base-to-novel performance.

Input: teacher features $\{\mathbf{v}_i^T\}$, caption embeddings $\{\mathbf{t}_{k,j}\}$; hyperparameters $(\zeta_s, \beta, \gamma, \varepsilon)$.

For each class k :

- 1) $\mathcal{B}_k \leftarrow \{i \mid y_i=k\}$; compute scores $s_{k,j} \leftarrow \frac{1}{|\mathcal{B}_k|} \sum_{i \in \mathcal{B}_k} (\mathbf{v}_i^T)^\top \mathbf{t}_{k,j}$.
- 2) $m_k \leftarrow \text{median}(\{s_{k,j}\}_j)$; $\Delta_{k,j} \leftarrow |s_{k,j} - m_k|$; $\text{MAD}_k \leftarrow \text{median}(\{\Delta_{k,j}\}_j)$; $z_{k,j} \leftarrow \Delta_{k,j} / (\text{MAD}_k + \varepsilon)$.
- 3) $\mathcal{J}_k \leftarrow \{j \mid z_{k,j} \leq \zeta_s\}$ // robust pruning of outlier captions

- 4) Compute weights $w_{k,j}$ for $j \in \mathcal{J}_k$ using Eq. 3, where the RS-Flag prior is added as a calibration term to the similarity scores before softmax normalization.

$$5) \mathbf{t}_k^{T*} \leftarrow \frac{\sum_{j \in \mathcal{J}_k} w_{k,j} \mathbf{t}_{k,j}}{\left\| \sum_{j \in \mathcal{J}_k} w_{k,j} \mathbf{t}_{k,j} \right\|_2} \quad // \ell_2\text{-normalization}$$

Output: $\{\mathbf{t}_k^{T*}\}_{k=1}^C$.

Selective prototype aggregation and robust pruning. The selective prototype aggregation algorithm (shown in the box above) is performed offline during training. Its core steps involve scoring caption candidates (Step 1), performing robust pruning (Steps 2-3), and then aggregating the remaining

Table 8. Detailed base-to-novel results (%) on six remote sensing datasets (ViT-B/32 student). Baselines: GeoRSCLIP [41], CoOp [43], CoCoOp [42], MMRL [13], MaPLe [20], PromptKD [24], and APPLeNet [28]. We report Base, Novel, and HM; Δ denotes the difference between **Ours** and the best-performing baseline for each metric.

(a) AID.				(b) RESISC-45.				(c) EuroSAT.			
Method	Base	Novel	HM	Method	Base	Novel	HM	Method	Base	Novel	HM
GeoRSCLIP [41]	71.96	76.90	74.35	GeoRSCLIP [41]	85.76	<u>81.17</u>	83.40	GeoRSCLIP [41]	80.60	82.00	81.29
CoOp [43]	<u>95.53</u>	66.41	78.35	CoOp [43]	90.19	74.97	81.88	CoOp [43]	91.09	68.94	78.48
CoCoOp [42]	94.83	68.03	79.22	CoCoOp [42]	92.97	74.97	83.01	CoCoOp [42]	92.61	73.25	81.80
MMRL [13]	95.27	70.40	80.97	MMRL [13]	94.10	77.58	<u>85.05</u>	MMRL [13]	<u>93.07</u>	<u>74.37</u>	82.68
MaPLe [20]	95.10	70.60	<u>81.04</u>	MaPLe [20]	93.50	76.50	84.15	MaPLe [20]	92.95	76.40	<u>83.87</u>
PromptKD [24]	94.90	70.00	80.57	PromptKD [24]	93.80	76.00	83.97	PromptKD [24]	92.70	75.80	83.40
APPLeNet [28]	94.60	69.50	80.13	APPLeNet [28]	93.00	75.00	83.04	APPLeNet [28]	92.20	74.10	82.17
Ours	95.80	<u>71.85</u>	82.11	Ours	<u>93.90</u>	83.17	88.21	Ours	94.90	77.15	85.11
Δ	+0.27	-5.05	+1.08	Δ	-0.20	+2.00	+3.16	Δ	+1.83	-4.85	+1.24

(d) WHU-RS19.				(e) UCMerced.				(f) PatternNet.			
Method	Base	Novel	HM	Method	Base	Novel	HM	Method	Base	Novel	HM
GeoRSCLIP [41]	85.62	<u>94.18</u>	89.70	GeoRSCLIP [41]	87.27	76.67	81.63	GeoRSCLIP [41]	57.38	67.59	62.48
CoOp [43]	93.08	88.54	90.75	CoOp [43]	94.88	60.22	73.68	CoOp [43]	82.22	58.06	70.14
CoCoOp [42]	93.08	90.84	91.95	CoCoOp [42]	93.69	63.11	75.42	CoCoOp [42]	83.94	53.95	68.94
MMRL [13]	<u>93.92</u>	90.14	91.99	MMRL [13]	<u>96.58</u>	70.67	81.62	MMRL [13]	89.56	59.00	74.28
MaPLe [20]	93.60	91.80	<u>92.69</u>	MaPLe [20]	96.20	72.20	<u>82.49</u>	MaPLe [20]	85.89	60.45	73.17
PromptKD [24]	93.40	90.90	92.13	PromptKD [24]	96.00	71.00	81.63	PromptKD [24]	91.21	<u>75.80</u>	83.50
APPLeNet [28]	93.20	90.50	91.83	APPLeNet [28]	95.80	71.20	81.69	APPLeNet [28]	<u>94.22</u>	74.20	<u>84.21</u>
Ours	96.85	94.45	95.63	Ours	97.90	<u>75.21</u>	85.07	Ours	94.50	77.83	86.16
Δ	+2.93	+0.27	+2.94	Δ	+1.32	-1.46	+2.58	Δ	+0.28	+2.03	+1.95

Table 9. Symbols and default/search ranges used in AVION. In all experiments we fix $K_p=30$, $\beta=10$, $\gamma=2$, $\zeta_s=3.0$.

Symbol	Meaning	Default / Search
N	# training images	–
C	# classes	–
D	image/text embedding dimension	inherited from the VLM
f_T, g_T	teacher image/text encoders	frozen
f_S, g_S	student image/text encoders	backbones frozen
\mathbf{v}_i^T	ℓ_2 -normalized teacher image feature for x_i	unit ℓ_2 -norm
\mathbf{t}_k^{T*}	teacher text prototype for class k	unit ℓ_2 -norm
\mathbf{v}_i^S	ℓ_2 -normalized student image feature for x_i	unit ℓ_2 -norm
\mathbf{t}_k^S	student text feature for class k	unit ℓ_2 -norm
K_p	# captions per class from <i>LLM-based domain prompting</i>	10–50
β, γ	weighting in <i>selective prototype aggregation</i> (Eq. 3)	$\beta \in [5, 20]$, $\gamma \in \{0, 2\}$
ζ_s	MAD-based pruning threshold (Eq. 9)	2.5–3.5
ε	numerical stability constant (Eq. 9)	10^{-8}
τ_s, τ_t	student/teacher logit scales	τ_t via grid search; τ_s learnable
τ	temperature of $\mathcal{L}_{\text{logit}}$ (Eq. 7)	$\tau=2$
$\lambda_{\text{img}}, \lambda_{\text{text}}, \lambda_{\text{logit}}$	loss weights	0.5, 0.5, 1.0 (fixed; see Appx. G)
$P^{(v)}$	# visual prompt tokens per layer	4–16
$P^{(t)}$	# text prompt tokens per layer	2–8
L_v, L_t	# prompt-injected layers (vision/text)	match ViT/Transformer depth

Table 10. Examples of LLM-generated candidate descriptions from our *LLM-based domain prompting* module, compared to standard simple templates. The generated candidates provide richer semantic and visual cues specific to remote sensing imagery.

Class Name	Simple Template	LLM-Generated Candidates
airport	a photo of an airport	<ul style="list-style-type: none"> - Overhead airport imagery reveals aprons (with parked aircraft at stands) adjacent to terminals, connected to the airfield via taxilanes and the taxiway system. - An aerial view of an airport showing multiple long, paved runways and taxiways. - Satellite imagery capturing a large airfield complex with terminal buildings and hangars.
industrial area	a photo of an industrial area	<ul style="list-style-type: none"> - A top-down view of an industrial zone characterized by large factory buildings and smokestacks. - Aerial imagery of a manufacturing plant complex with large warehouses and shipping depots. - A satellite photo showing a dense cluster of large-scale industrial structures and storage tanks.
commercial area	a photo of a commercial area	<ul style="list-style-type: none"> - An overhead view of a commercial district featuring multi-story office buildings and retail centers. - Nadir-view imagery of a dense downtown business area with high-rise buildings and streets. - An aerial photo of a shopping center or mall surrounded by a large, organized parking lot.
forest	a photo of a forest	<ul style="list-style-type: none"> - A vast expanse of dense, green forest canopy as seen from a satellite. - An aerial view looking straight down at a dense woodland of coniferous or deciduous trees. - A top-down remote sensing image of a large, contiguous area covered by trees.

candidates using the RS-Flag prior (Steps 4-5) to obtain the final teacher text prototype for each class.

The robust z -score used in Step 2 is computed using the median absolute deviation (MAD). Let $m_k = \text{median}(\{s_{k,j}\}_j)$, $\Delta_{k,j} = |s_{k,j} - m_k|$, and $\text{MAD}_k = \text{median}(\{\Delta_{k,j}\}_j)$. The z -score is defined as

$$z_{k,j} = \frac{\Delta_{k,j}}{\text{MAD}_k + \varepsilon}, \quad (9)$$

which downweights or removes outlier captions whose scores deviate strongly from the median.

E. Masking and Renormalization for $\mathcal{L}_{\text{logit}}$ in Base to Novel Training

Let $\mathcal{Y}_{\text{base}} \subset \mathcal{Y}$ denote the set of base classes and $\mathcal{Y}_{\text{novel}} = \mathcal{Y} \setminus \mathcal{Y}_{\text{base}}$ the set of novel classes. During base-to-novel training, we restrict the distillation distributions to base classes by masking scores for $\mathcal{Y}_{\text{novel}}$ and renormalizing over $\mathcal{Y}_{\text{base}}$:

$$\tilde{q}_{i,k}^{(T)} = \begin{cases} \frac{\exp(s_{i,k}^{(T)}/\tau)}{\sum_{k' \in \mathcal{Y}_{\text{base}}} \exp(s_{i,k'}^{(T)}/\tau)} & k \in \mathcal{Y}_{\text{base}}, \\ 0 & k \in \mathcal{Y}_{\text{novel}}, \end{cases} \quad (10)$$

$$\tilde{p}_{i,k}^{(S)} = \begin{cases} \frac{\exp(s_{i,k}^{(S)}/\tau)}{\sum_{k' \in \mathcal{Y}_{\text{base}}} \exp(s_{i,k'}^{(S)}/\tau)} & k \in \mathcal{Y}_{\text{base}}, \\ 0 & k \in \mathcal{Y}_{\text{novel}}. \end{cases} \quad (11)$$

Here $s_{i,k}^{(T)}$ and $s_{i,k}^{(S)}$ are the teacher and student logits for image x_i and class k , and τ is the distillation temperature used in $\mathcal{L}_{\text{logit}}$ (Eq. 7). The $\mathcal{L}_{\text{logit}}$ term then becomes

$$\mathcal{L}_{\text{logit}}(x_i) = \tau^2 \text{KL}(\tilde{q}_{i,\cdot}^{(T)} \parallel \tilde{p}_{i,\cdot}^{(S)}),$$

which ensures that novel classes neither appear in the denominator nor contribute to the divergence during training.

F. Complexity and Inference Overhead

We quantify the additional parameters and computational overhead introduced by AVION on top of a frozen GeoRSCLIP backbone. Unless otherwise stated, all numbers below correspond to our default ViT-B/32 student with deep prompts in both encoders.

Parameter count. For vision and text branches with widths D_v and D_t and L_v, L_t transformer layers that receive prompts, the total number of prompt parameters is

$$\#\theta_{\text{prompts}} = L_v P^{(v)} D_v + L_t P^{(t)} D_t,$$

where $P^{(v)}$ and $P^{(t)}$ denote the number of learnable prompt tokens per layer on the vision and text sides, respectively (see Tab. 9). In our main configuration (GeoRSCLIP ViT-B/32 student), the vision encoder has $D_v=768$, $L_v=12$, $P^{(v)}=8$, and the text encoder has $D_t=512$, $L_t=12$, $P^{(t)}=4$. Then

$$12 \cdot 8 \cdot 768 + 12 \cdot 4 \cdot 512 = 98,304$$

trainable prompt parameters, which is well below 1% of a ViT-B/32 backbone. All other backbone weights remain frozen; beyond these prompts, only a handful of scalar hyperparameters (e.g., the learnable logit scale τ_s) are updated.

FLOPs overhead (self-attention and MLP). Let N be the per-layer token count and P the number of prompt tokens added to that layer. The self-attention cost scales from N^2 to $(N+P)^2$, so the *relative* attention overhead is

$$r_{\text{attn}} \approx \frac{(N+P)^2 - N^2}{N^2} = 2 \frac{P}{N} + \left(\frac{P}{N}\right)^2.$$

The MLP cost scales approximately linearly with sequence length and therefore grows proportionally to P/N .

Examples (our setup). For the vision branch, ViT-B/32 at input resolution 224^2 has $N_v=49$ patch tokens; with $P^{(v)}=8$,

$$r_{\text{attn}}^{(v)} \approx 2 \cdot \frac{8}{49} + \left(\frac{8}{49}\right)^2 \approx 35.3\%,$$

and the per-layer MLP overhead is $\approx P^{(v)}/N_v \approx 16.3\%$. (We ignore the class token here for a rough estimate.) For the text branch, the CLIP text encoder uses $N_t=77$ tokens; with $P^{(t)}=4$,

$$r_{\text{attn}}^{(t)} \approx 2 \cdot \frac{4}{77} + \left(\frac{4}{77}\right)^2 \approx 10.7\%,$$

and the MLP overhead is $\approx P^{(t)}/N_t \approx 5.2\%$. Because ViT-B/32 has shorter vision sequences than ViT-B/16, the same P yields a larger *relative* attention overhead; reducing P or using shallower prompting (smaller L_v, L_t) lowers this cost. In practice, these per-layer increases translate into a moderate end-to-end FLOPs and latency overhead compared to the frozen backbone.

Runtime and memory. Table 11 reports the measured runtime of our ViT-B/32 student (frozen backbone + deep prompts). We report latency, throughput, and memory consumption over different batch sizes at 224^2 resolution. Throughput is computed as *batch size / latency*; exact numbers may vary across hardware and software stacks. The teacher is used only during training, so it incurs zero cost at inference.

Table 11. Runtime with ViT-B/32 student (frozen backbone + deep prompts). Teacher is train-time only and has zero inference cost. Throughput is computed as batch/latency; exact numbers may vary by hardware and software stack.

Setting	Batch	Res.	Lat. (ms)	img/s	Mem (MB)
Student	64	224^2	27.4	2334	1500
Student	256	224^2	109.7	2334	5800
Teacher (train-time only)	64	224^2	n/a	n/a	n/a

G. Hyperparameter Sensitivity Analysis

In this section, we provide a detailed justification of the hyperparameter choices used for our AVION framework, focusing on (i) our parameter selection protocol, (ii) the effect of loss weights (λ) and scheduling, and (iii) our choice of distillation temperature (τ).

Parameter Selection Protocol and Fixed Settings. To ensure robustness and avoid over-tuning, all hyperparameters were selected *once* on a validation split derived from the **AID** dataset’s base classes. These exact settings (e.g., learning rates, loss weights, warm-up schedule) were then frozen and applied to all six classification datasets and both retrieval datasets across all three experimental protocols (few-shot, base-to-novel, and retrieval). The strong performance across all tasks suggests the robustness of this single set of hyperparameters. Furthermore, following prior work on logit-based distillation [24], we use a default distillation temperature of $\tau=2$ and do not tune it as part of our selection process.

Analysis of Loss Weights and Scheduling. We conducted a detailed ablation study, summarized in Table 12, to val-

idate our final loss weight configuration ($\lambda_{\text{img}/\text{text}}=0.5$, $\lambda_{\text{logit}}=1.0$) and the 30% linear warm-up strategy on the $\mathcal{L}_{\text{logit}}$ term. The results lead to three key conclusions:

Table 12. Ablation on loss weights (λ) and scheduling strategies. We report the average harmonic mean (HM, %) for base-to-novel generalization.

Setting	λ_{img}	λ_{text}	λ_{logit}	Avg. HM
Only $\mathcal{L}_{\text{logit}}$	0	0	1.0	83.14
All 1.0 (2-stage)	1.0	1.0	1.0	85.47
All 1.0 (Warm-up)	1.0	1.0	1.0	86.91
Ours (Warm-up)	0.5	0.5	1.0	87.05

- The tri-aspect alignment losses are critical and complementary.** Relying only on $\mathcal{L}_{\text{logit}}$ results in a significantly lower HM (83.14%), indicating that the representation alignment \mathcal{L}_{img} and semantic alignment $\mathcal{L}_{\text{text}}$ play a critical role in achieving top performance.
- Our chosen weights ($\lambda_{\text{img}/\text{text}}=0.5$) provide a better balance.** Setting all three weights to 1.0 yields a strong 86.91% HM, but it is slightly outperformed by our final configuration at 87.05% HM. Comparing “All 1.0 (Warm-up)” and “Ours (Warm-up)” isolates the effect of λ_{img} and λ_{text} , suggesting that giving these embedding-level alignment terms a higher weight (1.0 vs. 0.5) can slightly over-regularize the student and hinder its optimal adaptation to the task.
- The 30% warm-up is the superior scheduling strategy.** Comparing “All 1.0 (2-stage)” (85.47%) and “All 1.0 (Warm-up)” (86.91%) isolates the impact of the scheduling policy. The smoother 30% warm-up schedule yields a clear HM improvement over the hard 2-stage scheme, and our final setting (“Ours (Warm-up)”) further reaches 87.05%. This supports our choice of a warm-up strategy for $\mathcal{L}_{\text{logit}}$ as a more stable and robust schedule.

H. Qualitative Analysis of RS-Flag

To empirically justify the reliability of the RS-Flag mechanism and demonstrate how it mitigates hallucinations, we use the “stadium” class as an example to visualize the normalized weights w obtained from Eq. (3), as shown in Figure 9. The candidates along the x-axis are ranked by their initial visual-textual similarity scores (blue bars).

As highlighted by the dashed circles, several candidates—most notably the top-ranked ones (indices 1, 2, and 3)—are significantly suppressed after applying the RS-Flag calibration (orange bars). This occurs because these candidates, despite having high initial visual alignment with the image, lack explicit remote sensing contextual features or contain ground-level negative words (i.e., RS-Flag=0). Taking index 3 as an example, a description like “A massive concrete ring structure surrounding a rectangular green field.” is not

inherently incorrect visually, but it lacks an explicit aerial perspective. Therefore, our mechanism does not directly eliminate it, but instead reduces its relative weight. This calibration allows candidates with stronger RS-awareness (e.g., indices 4, 5, 6, and 7), which receive a positive logit shift (RS-Flag=1), to correctly dominate the final aggregated prototype.

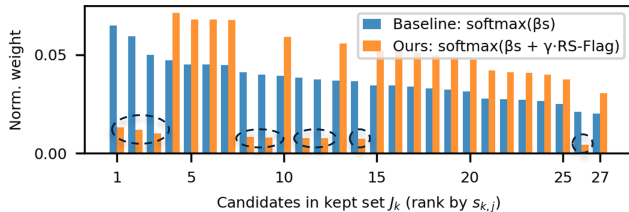


Figure 9. Qualitative analysis of the RS-Flag mechanism using the “stadium” class. Candidates are ranked by their initial similarity ($s_{k,j}$). The visualization compares the baseline softmax weights with our calibrated weights. Dashed circles highlight candidates (e.g., indices 1–3, 8–9, 11–12, 14, 26) that lack explicit remote sensing context and are consequently down-weighted to emphasize true RS-aware descriptions.

I. Cross-dataset Evaluation

To further validate the generalization capabilities of AVION and verify that it reduces source-domain overfitting, we conduct a cross-dataset evaluation. We train AVION under a 16-shot setting (using all classes) on the PatternNet dataset and report the zero-shot transfer performance on three target datasets: RESISC-45, UCMerced, and AID (all classes). For fairness, we re-implement all evaluated methods on the identical GeoRSCLIP (ViT-B/32) backbone.

As demonstrated in Table 13, AVION significantly outperforms APLeNet on the source domain (+5.46%) and consistently transfers better to unseen target domains: +2.88% on RESISC-45, +1.87% on UCMerced, and +1.59% on AID. Overall, AVION generalizes better across diverse remote sensing datasets, suggesting that our framework effectively mitigates the common issue of source-domain overfitting.

Table 13. Cross-dataset evaluation (%). Models are trained on PatternNet (16-shot) and evaluated zero-shot on targets. All methods utilize the GeoRSCLIP (ViT-B/32) backbone. ZS: Zero-shot.

Method	Source	Target		
	PatternNet	RESISC-45	UCMerced	AID
GeoRSCLIP (ZS)	60.17	71.89	79.72	73.72
APLeNet	86.63	73.25	80.18	76.40
AVION (Ours)	92.09	76.13	82.05	77.99

J. Ablation on LLM Domain Prompting

To ensure that the AVION framework is not overly sensitive to the specific large language model employed for domain prompting, we conduct an ablation study evaluating different offline LLM generators. Table 14 reports the average few-shot and base-to-novel generalization results across all six remote sensing datasets using text candidates generated by GPT-5, Llama-3.1-70B-Instruct, and our default Gemini 2.5 Flash.

The performance differences are marginal across all metrics. This stability confirms that AVION’s performance gains stem fundamentally from the architectural design of the verification and distillation mechanisms (e.g., RS-Flag and tri-aspect alignment), rather than relying on the idiosyncrasies of a specific language model.

Table 14. Ablation on offline LLM choices. We report average few-shot accuracy and base-to-novel generalization (Base, Novel, HM) in % across six RS datasets. The framework remains stable regardless of the LLM generator used.

Offline LLM	Few-Shot		Base-to-Novel		
	4-shot	16-shot	Base	Novel	HM
GPT-5	88.45	92.85	95.15	78.45	86.00
Llama-3.1-70B-Inst.	87.12	93.65	95.72	79.55	86.89
Gemini 2.5 Flash (Ours)	88.31	93.69	95.64	79.94	87.05

K. Comparisons on Broader Benchmarks

While AVION is explicitly tailored to address the unique challenges of aerial and satellite imagery, we also explore its scalability and general applicability on the broader, general-domain ImageNet benchmark.

For this experiment, we evaluate the base-to-novel generalization setting using a standard CLIP (ViT-B/16) student model. To adapt our pipeline to general-domain images, we modify the offline LLM generator query to a general template: “*In one sentence, describe the distinctive appearance of [CLASS].*” We generate 30 candidate descriptions per class using Gemini 2.5 Flash. Additionally, because ImageNet consists primarily of ground-level, human-centric photographs, we disable the RS-Flag filtering mechanism. Instead, the framework relies solely on the visual-textual similarity (Eq. (2)) and the MAD-based robust pruning for selective prototype aggregation.

As shown in Table 15, our offline-teacher-to-student distillation paradigm remains highly effective outside the remote sensing domain. When guided by a ViT-H/14 CLIP teacher, AVION outperforms the recent state-of-the-art general prompt tuning method MMRL in terms of the Harmonic Mean (HM). This suggests that the core mechanism of distilling semantically rich, visually verified prototypes is a

versatile approach that generalizes well beyond aerial contexts.

Table 15. Base-to-novel generalization (%) on the ImageNet benchmark. The student model is CLIP (ViT-B/16). AVION demonstrates competitive transferability on general-domain images without the RS-Flag constraint.

Method	Base	Novel	HM
MMRL	77.90	71.30	74.45
AVION (Teacher: ViT-L/14)	77.27	74.02	75.63
AVION (Teacher: ViT-H/14)	79.15	74.79	76.94